FIBRIL PAINT TO DETECT AMYLOIDS AND DETERMINE FIBRIL LENGTH

Júlia Aragonès Pedrola[1, 2, 3, #], Françoise A. Dekker[1, 2, 3, #], Tommaso Garfagnini[4,5] Guy Mayer[4], Margreet B. Koopman[1, 2, 3], Menno Bergmeijer[2, 6], Friedrich Förster[2,6], Jeroen J. M. Hoozemans[7], Henrik Jensen[8], Assaf Friedler[4, *], Stefan G. D. Rüdiger[1, 2, 3 *]

[1] Cellular Protein Chemistry, Bijvoet Center for Biomolecular Research, Utrecht University, Padualaan 8, 3584CH Utrecht, The Netherlands.

[2] Science for Life, Utrecht University, Padualaan 8, 3584CH Utrecht, The Netherlands.

[3] Protein Chemistry of Disease, Department of Chemistry, Utrecht University, Padualaan 8, 3584CH Utrecht, The Netherlands.

[4] Institute of Chemistry, The Hebrew University of Jerusalem, Edmond J. Safra Campus at Givat Ram, Jerusalem 9190401, Israel.

[5] Present address: School of Cellular and Molecular Medicine, University of Bristol, BS8 1TD Bristol, United Kingdom

[6] Structural Biochemistry, Bijvoet Centre for Biomolecular Research, Utrecht University, Utrecht, The Netherlands

[7] Department of Pathology, Amsterdam Neuroscience, Amsterdam UMC-location VUmc, Amsterdam, The Netherlands

[8] Fida Biosystems ApS Generatorvej 6 A+B 2860 Søborg Denmark

[#] These authors contributed equally

[*] Corresponding authors

Running title

Fibril Paint

Abstract

Protein aggregation is related to the development of amyloid diseases, such as Alzheimer's Disease and Huntington's Disease. It is of great importance to detect aggregates at the earliest stage possible, which is a prerequisite for early diagnosis. Here, we present a method to monitor protein fibril size from early aggregation steps. We designed a peptide, FibrilPaint1, that specifically recognises and fluorescently labels various fibrils from diseases, but not their monomeric precursors. In combination with Flow Induced Dispersion Analysis, a microfluidics technology, we determined the molecular size of amyloid fibrils with sub-microliter sample volumes. FibrilPaint1 specifically detects structurally unrelated fibrils from Huntingtin and Tau, including *ex vivo* samples derived from Alzheimer's Disease, Frontotemporal Dementia and Corticobasal Degeneration patients. The ability to recognise multiple amyloids but not monomeric precursors makes FibrilPaint1 a novel tool for diagnostic applications for amyloid diseases.

Keywords

Protein aggregation, peptide design, Flow Induced Dispersion Analysis (FIDA), protein folding, protein fibrils, neurodegeneration, diagnosis, Tau, Huntingtin

Introduction

Protein aggregation into amyloid fibrils characterizes the development of neurodegenerative diseases, affecting 55 million people worldwide (Long et al., 2023; Organization, 2017). In these diseases, aggregated proteins are hypothesised to have a causative relation with the disease onset. For example, Tau fibril formation is highly related to the progression of tauopathies, including Alzheimer's Disease (AD), Frontotemporal Dementia (FTD), or Corticobasal Degeneration (CBD) (Ballatore et al., 2007; Spillantini & Goedert, 2013). In the case of Huntingtin (Htt), its fibrillation is directly correlated to the onset and progression of Huntington's disease (HD) (Andrew et al., 1993; Saudou & Humbert, 2016).

Currently, neurodegenerative diseases lack causal treatment, leading to a significant challenge in healthcare. Antibodies, such as Lecanemab and Aducanumab have shown promise in treatment (Day et al., 2022; Van Dyck et al., 2023). However, these therapies include side effects such as brain edema or sulcal effusion hemorrage. These side effects also manifest as amyloid-related imaging abnormalities (Day et al., 2022; Shi et al., 2022; Shi, Murzin, et al., 2021; Van Dyck et al., 2023). The most common diagnosis techniques, such as phenotypical behaviour and brain imaging, correlate with massive accumulation of aggregated protein into amyloid fibrils, which occurs in a stage where the brain is irreversibly damaged. (Association, 2016; Bradford et al., 2009; Thal et al., 2013). It is of great importance to develop techniques that specifically recognise fibrillar structures and early aggregated species, but not free monomers.

A range of techniques can detect amyloid fibrils both formed *in vitro* and extracted *ex vivo*. Negative staining and cryo- electron microscopy are useful for assessing the morphology of the formed fibrils, as well as the branching, width, and length (Shi, Zhang, et al., 2021; Sunde & Blake, 1997) Dyes, such as Thioflavin T (ThT) and Congo Red, are qualitative methods used for the identification of amyloid structures *in vitro* and histology staining (Elghetany & Saleem, 1988; Howie et al., 2008; Vassar & Culling, 1959). Antibodies, large biologics of 150 KDa, are capable of recognising the specific protein forming the aggregate (Ko et al., 2001; Ksiezak-Reding et al., 1987; Sevigny et al., 2016; Van Dyck et al., 2023). However, antibodies are expensive and difficult to modify. Smaller compounds

have higher chances to reach targets in the brain and are easier to design, which is exploited for the development of PET tracers, which are radioligands used for diagnostic purposes (Mueller et al., 2020; Shi, Murzin, et al., 2021). There is a strong medical need for such diagnostic tracer drugs able to early identify pathological protein fibrils in patients, such as binders against Tau.

Tracing fibrils requires the development of molecules that specifically bind fibrils. Tau accumulation is linked to a variety of Tauopathies, among which is AD (Bejanin et al., 2017; Iaccarino et al., 2021; Jack et al., 2019; Merz et al., 2023; Ossenkoppele et al., 2018; Ossenkoppele et al., 2016). In 2020, imaging agent Tauvid ([18F]-flortaucipir) was approved by the FDA (Commissioner, 2020; Jie et al., 2021; Ossenkoppele et al., 2018; Xia et al., 2013). Tauvid is currently the only PET tracer approved for diagnosing living patients, with results that can discriminate disease as well as stage of the disease (Jie et al., 2021; Leuzy et al., 2020; Merz et al., 2023; Mohammadi et al., 2023). Tracers for other aggregating proteins are also in development. For Huntingtin, the protein that aggregates in HD, tracers have passed tests on *ex vivo* samples (Delva et al., 2022; Herrmann et al., 2021; Liu et al., 2021; Liu et al., 2020; Matlahov et al., 2022). Even though PET tracers remain a valuable tool in diagnosis and in monitoring neurogenerative diseases directly in the brain, they present some limitations such as costs and limited accessibility (Ossenkoppele & Hansson, 2021). Transitioning to fluid-based biomarkers presents a great promise in advancing diagnosis of neurodegenerative diseases (Alcolea et al., 2023; Hansson et al., 2022; Teunissen et al., 2022). Brain constituents can for example end up in the cerebrospinal fluid (CSF), providing sometimes earlier signs of accumulation of aggregates than PET tracers, although the procedure of sampling CSF is invasive (Martí-Martínez & Valor, 2022; Palmqvist et al., 2016).

Here we present FibrilPaint1, a peptide that specifically recognises the repetitive nature of amyloid fibrils, acting as fibril paint. It can fluorescently stain amyloid fibrils of Tau and Huntingtin, which differ in structure and sequence, but not the non-aggregated monomeric form. The staining activity of FibrilPaint1 is enhanced by combination of π-stacking and H-bonding interactions (Ferrari et al., 2020; Garfagnini et al., 2022). These interactions are crucial for the recognition of fibrils but not monomers, increasing the binding affinity for the aggregated forms. In

combination with Flow Induced Dispersion Analysis (FIDA), we determined the hydrodynamic radius of the aggregated species. As a result, we can detect the size of recombinant aggregates during the whole aggregation process and patient-derived fibrils.

Results

Development of a multi-targeting method to detect amyloids

We set out to develop a method to detect multiple amyloid fibrils (**Fig. 1**). Our strategy is established using Tau and Huntingtin (Htt), two aggregating proteins that are unrelated in sequence and structure. Tau is an intrinsically disordered protein that can aggregate into distinct conformations when it is detached from the axons of neurons (Arendt et al., 2016; Scheres et al., 2020; Stelzl et al., 2022) HD is an autosomal inherited disorder, where the start of aggregation correlates with the length of expansion of a glutamine stretch in the exon 1 of the Htt protein (Elena-Real et al., 2023; Isas et al., 2017; Isas et al., 2021; Lieberman et al., 2019).

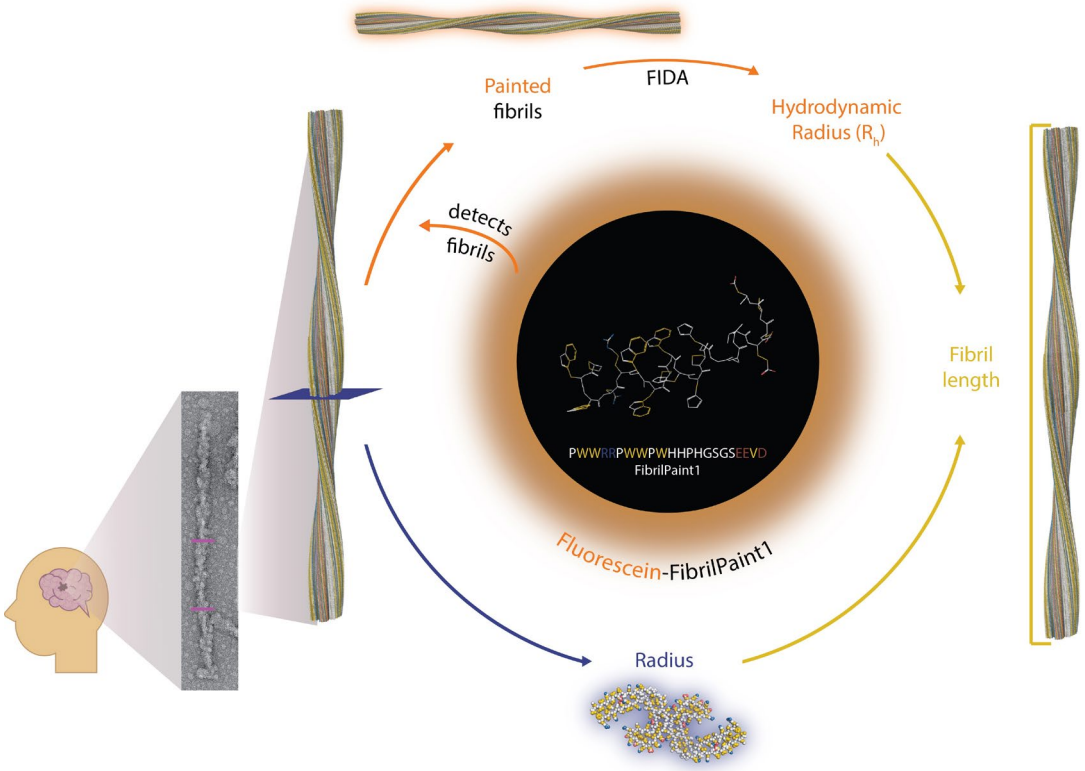

Figure 1 **Abstract Figure: FibrilPaint1 to detect the presence of fibrils and determine fibril size**. FibrilPaint1 (in circle) detects the presence of amyloid fibrils. Through its Fluorescein-tag, binding works as fluorescent staining of fibrils (orange pathway). The stained fibils can be analysed with FIDA to get the hydrodynamic radius (R_h) of the fibril population. If the structure of the fibril is known, this can be used to determine the radius of the fibril (blue pathway). Otherwise, estimations can be made. Combined, these data can be converted to give the fibril length (yellow pathway).

Our previous work described the development of a family of peptides that inhibit aggregation of several unrelated proteins at early stages (Garfagnini et al., 2022). Based on that, we developed a set of four new peptides. To enhance the peptide binding to aggregates, we further increased the density of π-stacking and H-bonding residues of some of the peptides (Ferrari et al., 2020; Garfagnini et al., 2022). We added a negative EEVD sequence C-terminally with a GSGS spacer, creating two oppositely charged sections, with a positively charged N-terminal region and a negatively charged C-terminus. The EEVD sequence may also serve as adaptor to recruit protein quality control factors that specifically recognise this sequence via a TPR domain, which is potentially interesting for follow-up studies (Scheufler et al., 2000; Zheng & Shabek, 2017). We added a fluorescein group (Fl-) at the N-terminus, which facilitates detection. We varied the net charge and the number of aromatics in the peptides. This further optimization resulted in a set of four 22-residue long peptides with different charge, number of aromatics and uneven distribution of the different types of residues (**Table 1**). Designed to make fibrils visible, we call this class of peptides FibrilPaints. FibrilPaint1 and FibrilPaint2 have Arginine residues on positions 4 and 5, whereas FibrilPaint3 and FibrilPaint4 have Aspartates. FibrilPaint1 and FibrilPaint4 have Histidines on positions 11 and 12where FibrilPaint2 and FibrilPaint3 have Threonines.

Name peptide	Sequence	Net charge	MW (kDa)	Tht inhibition	Fibril binding	R_H (nm)
aB Peptide*	PWIRRPFFPFHSPSR	+3	1.93	Yes	-	
WTG peptide*	GWWRRGWWGWTTGTR	+3	1.95	Yes	-	
FibrilPaint1	(Fl)-PWWRRPWWPWHHPHGSGSEEVD	-1	2.82	Yes	Yes	1.7
FibrilPaint2	(Fl)-PWIRRPWWPWTTPTGSGSEEVD	-1	2.64	Yes	No	1.7
FibrilPaint3	(Fl)-PWWDDPWWPWTTPTGSGSEEVD	-5	2.63	Yes	No	1.7
FibrilPaint4	(Fl)-PWWDDPWWPWHHPHGSGSEEVD	-5	2.74	Yes	No	1.7

Table 1 **Peptide names and sequences.** Peptides indicated with * are first generation peptides (Garfagnini et al., 2022). (Fl) at the N-terminal of the sequence indicates fluorescein, which is not considered when calculating the molecular weight or number of aminoacids. Aminoacid colouring based on YRB colous (hydrophobic residues, yellow; negatively charged residues, red; positively charged residues, blue) (Hagemans et al., 2015).

The four peptides inhibit Tau and Htt amyloid aggregation

We assessed whether FibrilPaint peptides 1 to 4 could interact with aggregate species of multiple proteins. To do so, we tested the inhibitory capacity of the peptides on the amyloid aggregation of two unrelated proteins, Tau Repeat

Domain (Q244-E372, TauRD) with the pro-aggregation mutation ΔK280, and Huntingtin Exon 1 comprising a 44 residues-long polyglutamine stretch (HttEx1Q44). We performed a ThT assay, an established method to monitor protein fibrils formation, in which the fluorescent dye ThT emits fluorescence upon binding to fibrils (Vassar & Culling, 1959). The four FibrilPaint peptides strongly inhibited the aggregation of 20 μM Tau-RD aggregation at substoichiometric concentration in a dose-dependent manner (**Fig. 2A-D**). At 2 μM, FibrilPaint1 was the most effective inhibitor, lowering the fluorescence intensity in the plateau by 92%, followed by FibrilPaint4 (90%), FibrilPaint2 (86%) and FibrilPaint3 (66%).

All FibrilPaints also inhibited aggregation of HttEx1Q44 at 20 μM in a dose-dependent manner, although less potently than TauRD (**Fig. 2E-H**). Here, FibrilPaint4 had the strongest effect, lowering the fluorescence intensity of the plateau with 74% at a concentration of 2 μM. FibrilPaint2 (55%), FibrilPaint3 (54%) and FibrilPaint1 (30%) inhibited aggregation of the polyglutamine protein to a significant extent, too. Overall, the four peptides inhibit amyloid aggregation of both TauRD and HttEx1Q44 at substoichiometric concentrations. This is remarkable as both proteins are entirely unrelated in sequence and the only common property is the formation of amyloid fibrils.

FibrilPaint1 binds to Tau and Htt fibrils

Next, we screened the four FibrilPaint peptides for direct binding to TauRD and HttEx1Q44 fibrils (**Fig. 2I, J**). To do so, we developed an application of FIDA to determine the size of amyloid aggregates. With FIDA, fluorescently labelled samples of interest is passed through a long capillary under pressure. The sample passes a detector window, resulting in a size-dependent diffuse profile. Smaller species diffuse faster and bigger ones slower, resulting in a narrow or broad dispersion fluorescent signal. Since FIDA relies on the physical diffusion properties of the sample, we can measure the hydrodynamic radius (R_h) of labelled species from the fluorescent signal. (He & Niemeyer, 2003; Miller, 1924). The R_h is a parameter corresponding to the size and shape of a molecule or a complex in solution. It is the radius of the sphere created by the tumbling particle.

R_h values can be estimated from the structural coordinates, either by experimental methods or by predictions such as AlphaFold (**Table 2**).

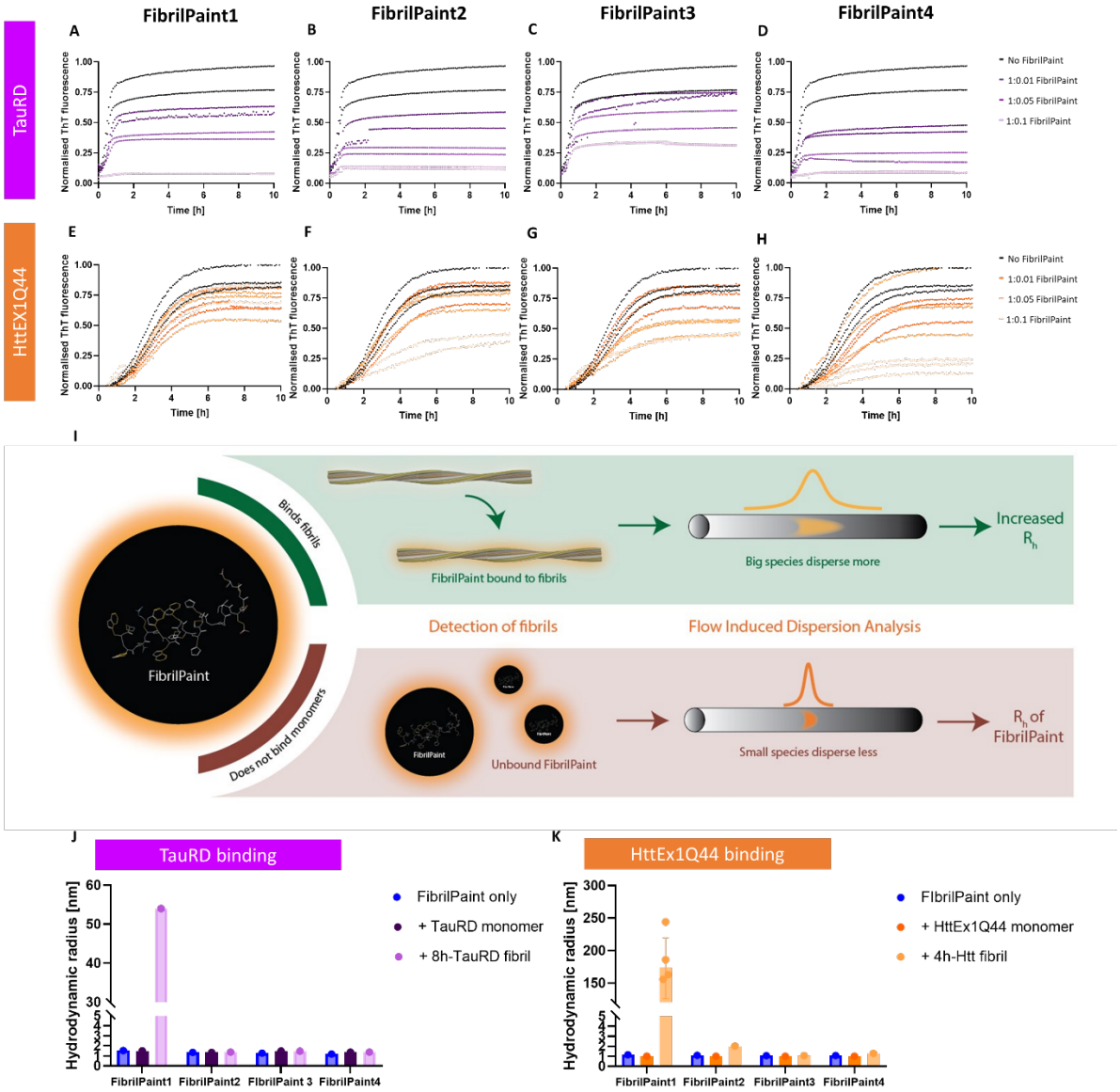

Figure 2. **FibrilPaint1 is a specific label for protein fibrils**. Inhibition of 20 µM TauRD (A-D) and 20 µM HttEx1Q44 (E-H) aggregation by 2-0.2-0.02 µM FibrilPaint1 (A, E), FibrilPaint2 (B, F), FibrilPaint3 (C, G) and FibrilPaint4 (D, H). All peptides lower the end-plateau in a dose-dependent manner for both TauRD and HttEx1Q44 aggregation. Binding of the peptides is evaluated with FIDA (I). If a FibrilPaint binds, this leads to a bigger species, which disperses more in FIDA leading to an increase in the perceived R_h (green box). If there is no binding, the R_h remains the same as the R_h of FibrilPaint only (red box). Binding of FibrilPaint to monomeric or fibrillar TauRD (J) or HttEx1Q44 (K) (FibrilPaint peptide only, blue; Tau-RD monomers, dark purple; HttEx1Q44 monomers, dark orange; Tau-RD fibrils, light purple; HttEx1Q44, light orange).

Table 2 **Protein structures and their predicted hydrodynamic radii**. The number of residues and the molecular weight are given for the total structure as available in the PDB. If structures are available, the included 1 layer R_h is the R_h a structure would have if it could fold in its fibrillar conformation with just one layer.

Protein structure	PDB code	Nr. residues	MW (kDa)	Predicted R_h (nm)		Origin prediction
				1 layer	5 layers	
Snake recombinant Tau	6QJH	177	18.67	2.29	3.49	Cryo-EM (Zhang et al., 2019)
Twister recombinant Tau	6QJM	144	15.57	1.73	2.68	Cryo-EM (Zhang et al., 2019)
Jagged recombinant Tau	6QJP	144	15.57	1.75	2.70	Cryo-EM (Zhang et al., 2019)
TauRD monomer		128	14.21	4.16		AlphaFold
Tau AD Paired helical filament	5O3L	730	79.40	3.33	4.33	Cryo-EM (Fitzpatrick et al., 2017)
Tau AD straight filament	5O3T	730	79.40	3.29	4.34	Cryo-EM (Fitzpatrick et al., 2017)
FTD narrow filament	6GX5	282	30.41	2.84	4.32	Cryo-EM (Falcon et al., 2018)
CBD type I	6TJO	321	137.76	2.67	4.07	Cryo-EM (Falcon et al., 2019)
CBD type II	6VH7	642	69.65	4.12	6.25	Cryo-EM (Falcon et al., 2019)
HttEx1Q44 monomer		120	13.82	3.4		AlphaFold
Luciferase	1LCI	550	60.82	3.35		X-Ray (Conti et al., 1996)

Determining the R_h for aggregating species requires a compound that labels the aggregate without altering its properties. The binding of the fluorescently labelled FibrilPaint peptide to protein fibrils increases the R_h value, as the peptide now tumbles together with the larger fibril (**Fig. 2I**). We determined the R_h of FibrilPaint1 to 4 in this set-up, revealing an R_h of 1.7 nm each (**Table 1**). To measure the R_h of fibril complexes, we incubated pre-formed fibrils together with each of the four peptides in a 1:100 peptide:monomer ratio. The excess of fibril was intended to minimise the presence of free peptide.

Testing the FibrilPaint peptides for binding to TauRD fibrils that aggregated for 8 h showed that FibrilPaint1 binds strongly, increasing the average R_h value from 1.5 nm to 54 nm (**Fig. 2J**). Importantly, incubation of FibrilPaint1 with TauRD monomer did not result in an increased R_h value, indicating that it does bind specifically to the fibril but not to the monomer (**Fig. 2C, J**). The binding of FibrilPaint2 to 4 to TauRD fibrils was not sufficiently stable to fluorescently label them effectively. It is interesting that only FibrilPaint1 binds strongly enough to act as a non-covalent label, given that all FibrilPaint peptides inhibit aggregation of TauRD. This indicates that high affinity to fibrils exceeds the demands required for prevention of aggregation, and fibril recognition and inhibition are two different properties.

Testing the FibrilPaint peptides for labelling of HttEx1Q44 fibrils resulted in remarkably similar results. The average R_h of FibrilPaint1 in the presence of HttEx1Q44 fibrils that aggregated for 4 h increased from 1.7 nm to 120 nm, while it did not bind to the monomer (**Fig. 2K**). FibrilPaint peptides 2-4 are also ineffective in binding HttEx1Q44 (**Fig. 2K**). Thus, it is a unique property of FibrilPaint1 to bind and fluorescently label protein fibrils of unrelated sequence, while not binding to the monomer.

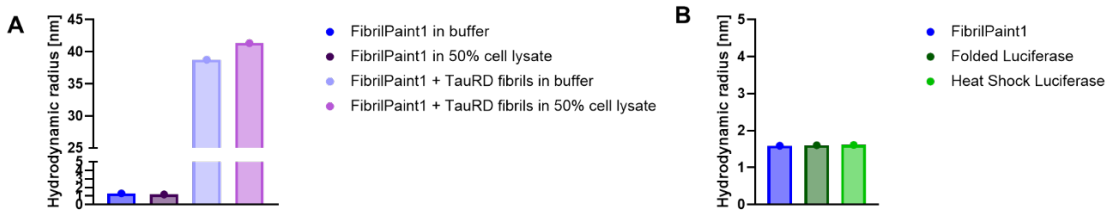

Figure 3 **FibrilPaint1 is specific for amyloid aggregates.** A) Binding of 0.2 µM FibrilPaint1 to TauRD fibrils in presence of 50% cell lysate or buffer. In presence of cell lysate, FibrilPaint1 has a size of 1.7 nm, incubated with 20h-TauRD fibrils has an average size of 39 nm. In buffer, FibrilPaint1 has a size of 1.7 nm, incubated with 20h-TauRD fibrils has an average size of 41 nm. B) No binding of 0.2 µM FibrilPaint1 to amorphous aggregated Luciferase by heat shock. FibrilPaint1 has a size of 1.7 nm, incubated with heat shock luciferase the size remains the same. (FibrilPaint1 peptide only, blue; cell lysate, dark purple; Tau-RD fibrils in buffer, light blue; Tau-RD fibrils in cell lysate, light purple; folded luciferase, dark green; heat-socked luciferase; light green).

FibrilPaint1 is amyloid-specific

We investigated whether FibrilPaint1 binds to fibrils without perturbance by other biomolecules or cellular components. We tested its ability to specifically recognise TauRD fibrils in presence of an abundance of other cellular proteins, by adding *E. coli* cell lysate. We incubated pre-formed 20 h TauRD fibrils together with FibrilPaint1 in a 1:100 ratio in 50% cell lysate. Under these conditions, FibrilPaint1 shows an increased size of 39 nm, which is consistent with the R_h of 41 nm measured from the same fibrils in buffer (**Figure 3A**). When incubating FibrilPaint1 alone in cell lysate, the size remains the same as FibrilPaint1 alone (**Figure 3A**). Thus, FibrilPaint1 specifically recognises fibrils in a complex cellular mixture.

Next, we tested whether binding of FibrilPaint1 to aggregates requires fibrillar structures. We used Luciferase as an established paradigm for non-amyloid aggregates (Parsell et al., 1994). Luciferase is a globular 61 KDa protein with a R_h of 3.4 nm (**Table 2**) that forms amorphous aggregates when denatured by heat shock. We incubated FibrilPaint1 together with heat-shocked Luciferase in a 1:100 ratio. The R_h of FibrilPaint1 in the FIDA measurement is not affected by the presence of luciferase aggregates (**Figure 3B**). This indicates that FibrilPaint1 does not bind to amorphous luciferase aggregates. Together, these data demonstrate that FibrilPaint1 binds specifically to amyloid fibrils, undisturbed by the presence of other biomolecules.

Monitoring fibril kinetics

We then set out to monitor aggregation kinetics following the increasing R_h using FibrilPaint1 and FIDA, for both TauRD and HttEx1Q44 (**Fig. 4A, E**). After 0.5 h, the aggregation reaction of TauRD resulted in an increase of the averaged R_h from 1.7 nm to 2 nm. All species measured at t = 0.5 h had the same size, indicating full binding of FibrilPaint1, without any dissociation taking place. No larger species were present at that timepoint. TauRD aggregation continued, and rapidly increased to an R_h 5 nm after 2 h (**Fig. 4A**). Fibril sizes measured were also more heterogeneous, indicating the presence of multiple aggregates with

varying lengths. Only the largest species were plotted **(Fig. 4A)**. TauRD aggregation reached a plateau at an R_h value of 45 nm after 8 h.

With the radius of the fibril, we can calculate its length using the Stoke-Einstein equation (**Sup. Fig. 1**) (He & Niemeyer, 2003; Miller, 1924). TauRD has an estimated radius between 2 and 2.5 nm, assuming its radius approaches the one of FL-Tau (**Table 2**). When aggregating, fibrils extend through a cylinder-like pattern, and the R_h must be converted to fibril length through the molecular weight and radius of gyration (**Sup. Fig. 1**) (He & Niemeyer, 2003; Yoshizaki & Yamakawa, 1980). This would mean that the plateau value of TauRD fibrils of 45 nm corresponds to fibril length of 436 to 466 nm, which is consistent to the length measured with ns EM (**Sup. Fig. 2**)

For HttEx1Q44, R_h increased to 5 nm after 1 h. This already exceeds the predicted R_h of the unfolded monomeric structure of HttEx1Q44, which is estimated to be 3.4 nm (**Table 2**). Therefore, this species consists of multiple monomers. Aggregation then exponentially increased up to an average R_h of 500 nm after 7 h (**Fig. 4E**). As the particle size reached the upper limit of the FIDA measurement, we could not determine the plateau value.

We monitored the aggregation process in parallel with the established ThT assay, in the fluorescence plate reader, for both TauRD and HttExon1Q44 (**Fig. 4B, E**). The ThT fluorescent signal rises immediately after addition of heparin to TauRD and increases rapidly reaching a plateau already after 4 h (**Fig. 4B**). The increase of the ThT fluorescent signal was faster than what we observed in the FIDA measurements using FibrilPaint1 (**Fig. 4A**). It suggests that formed fibrils may already be saturated by ThT but are still growing in length. We obtained similar results for HttEx1Q44. The ThT revealed a lag-phase of approximately 2 h and a plateau after 5 h of aggregation (**Fig. 4E**), while the size of the fibrils still increased (**Fig. 4D**). The aggregation of HttEx1Q44 was more aggressive than aggregation of TauRD, and resulted in larger fibrils. This observation may reflect that the fibrils form larger fibril clusters sticking the fibrils together. We conclude that both methods are complementary, with the ThT assay providing a signal representing the presence of amyloid fibrils while the FIDA measurements provides in addition a readout for the length of the fibrils that goes beyond the early aggregation phase.

Characterising fibril shape

Next, we set out to compare the average fibril size obtained by FIDA data with single particle EM images. We used negative stain EM imaging to characterise the shape of the TauRD fibrils after 24 h aggregation and HttEx1Q44 fibrils after 6 h (**Fig. 4C, F**). TauRD fibrils appeared as long, single, fibrillar structures (**Fig. 4C**). The length of the Tau fibrils varied strongly and was on average 500 to 600 nm (**Sup. Fig. 2**), bigger than our FIDA observations. This is as expected, as smaller fibrils are excluded due to the lower detection limits of the technique. On the contrary, HttEx1Q44 fibrils formed larger clusters of fibrils (**Fig. 4F**) (Boatz et al., 2020; Isas et al., 2021; Matlahov et al., 2022; Nazarov et al., 2022). We noted a large variation between the sizes of these clusters: from just a few fibrils of 50-100 nm to enormous clusters of several µm in width. A representative shape formed by these clusters is around 800 nm long and 200 nm wide (**Fig. 4F**). Since this shape is more spherical than singular fibrils, it would result in an R_h of 400 nm, which is consistent with the R_h of 300-500 nm in FIDA experiments. These clusters explain the rapid increase in size detected with FIDA and reaching the upper limit of the FIDA measurement.

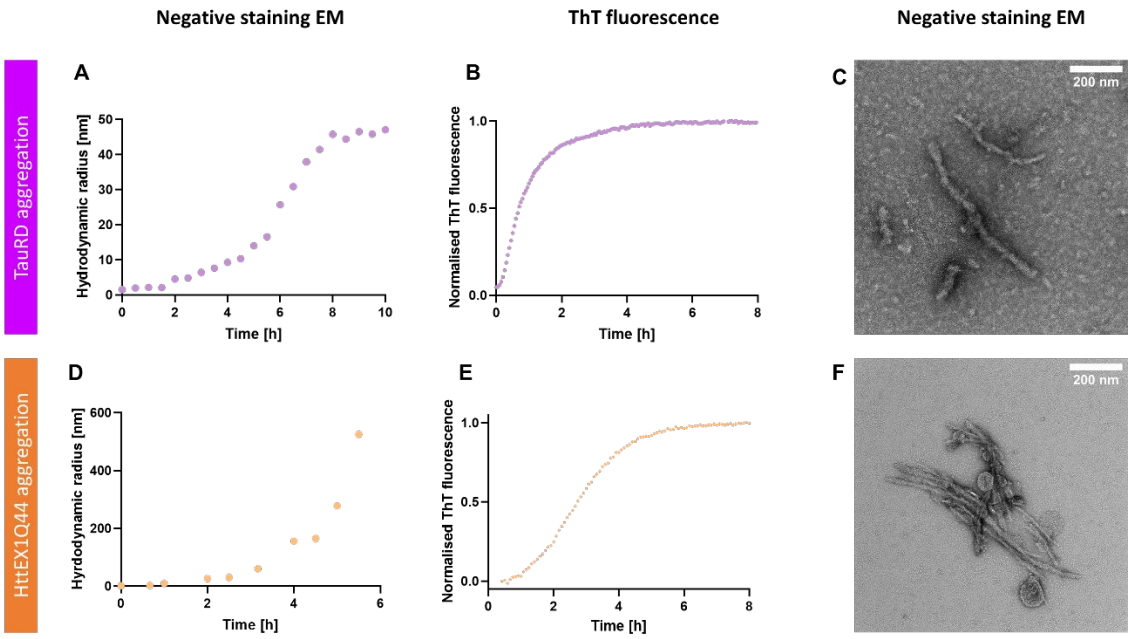

Figure 4 **Aggregation of TauRD and HttEx1Q44 over time.** Hydrodynamic radius of aggregates as determined with FIDA for TauRD (A) and HttEx1Q44 (D). In parallel experiments, aggregation was monitored with a ThT assay (B, E) for TauRD and HttEx1Q44. The end-product of TauRD was pictured with negative stain EM after 24 h (C) and for HttEx1Q44 after 6 h (F). (Tau-RD aggregation, purple; HttEx1Q44 aggregation, orange.)

FibrilPaint1 determines the size of inhibited species

Next, we set out to analyse how large the ensemble of the inhibited aggregated species become. With the ThT assays, we saw that in the presence of FibrilPaint1, TauRD seems to be completely inhibited, whereas HttEx1Q44 aggregation slowed down (**Fig. 2A, E**) We took samples at various timepoints of the stalled aggregation reaction and measured them in FIDA (**Fig. 5**). In presence of FibrilPaint1, TauRD aggregation reached a R_h of 3.5 nm after 2 h incubation. This species of 3.5 nm remained stable for 8 h (**Fig. 5A**). Interestingly, the fibrils were too small to be visible in negative staining EM images (**Fig. 5C**). Under the same inhibiting conditions, HttEx1Q44 aggregated to an average size of 28 nm in presence of FibrilPaint1, remaining stable over 8 h (**Fig. 5B**). Negative staining EM showed that Htt fibrils had much more space between them upon addition of FibrilPaint1, showing more unbundled fibril shapes (**Fig. 5C**).

Although FibrilPaint1 inhibits both TauRD and HttEx1Q44 aggregation, it is evident that the inhibited state of HttEx1Q44 fibrils include more layers than TauRD fibrils. TauRD aggregates to a R_h of 3.5 nm, which is estimated to be 5 layers (**Table 2**). The 28 nm R_h of HttEx1Q44 is a bit more difficult to convert. Assuming all fibrils are unbundled now, and we have a radius of 3 to 3,5 nm, we can estimate the fibril length of Htt to be between 220 nm and 280 nm (**Fig. 5C, Sup. Fig. 2**)(Helabad et al., 2023). FIDA is therefore a suitable method to characterise the state of inhibited fibrils and shows consistent data with ThT and nsEM images (**Fig. 5**).

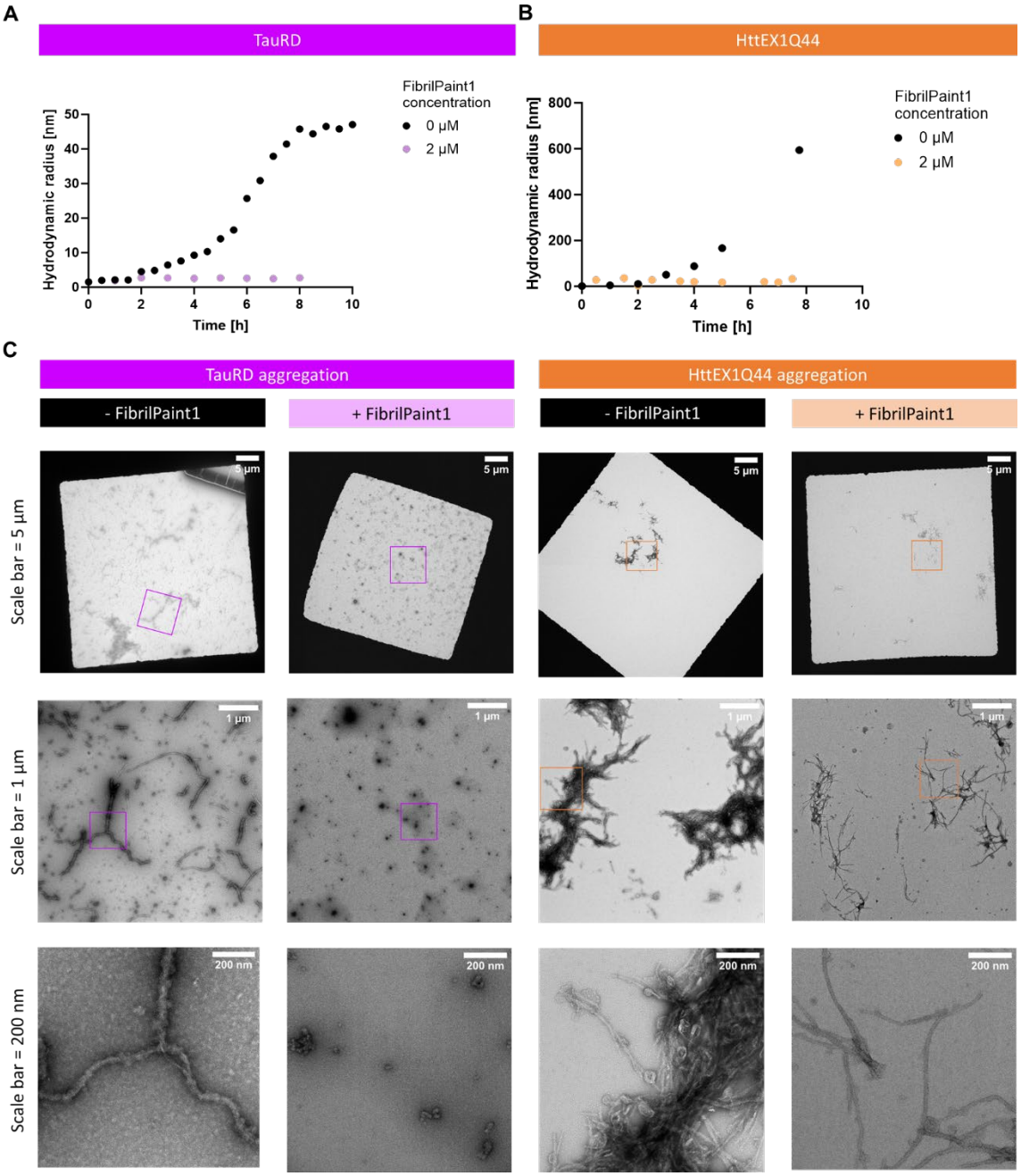

Figure 5 **Fibril inhibition over time by FibrilPaint.** Aggregation of TauRD (A) and HttEx1Q44 (B) in presence or abscence of 2 µM FibrilPaint1. In presence of FibrilPaint1, R_h remains 3 nm for TauRD (A) and 28 nm for HttEx1Q44 (B). Both datasets are representative experiments for three independent performed experiments. The end product of TauRD with and without FibrilPaint1 was imaged by negative stain EM after 24 h (C), and after 6 h for HttEx1Q44 (D). (Tau-RD inhibition by FibrilPaint1, purple; HttEx1Q44 inhibition by FibrilPaint1, orange.)

FibrilPaint1 for monitoring patient-derived fibrils

Given that FibrilPaint1 specifically binds amyloid fibrils, it may have potential for diagnostic tracing of protein fibrils in patients. This would require that FibrilPaint1 would recognise patient-derived fibrils. Interestingly, cryo-EM structures of Tau fibrils show that their shape differs for the various tauopathies, and heparin-induced recombinant fibrils (Scheres et al., 2020) (**Fig. 6B**). As potential reporter for Tau fibrils, it was important to assess the ability of FibrilPaint1 to recognise patient-derived fibrils of several tauopathies.

We set out to measure *ex vivo* Tau fibrils from three different tauopathies. We purified fibrils from deceased patients diagnosed with CBD, FTD and AD. Monomeric Tau undergoes different post-translational alternative splicing in different diseases, leading to six different isoforms, with either four (4R) or three (3R) repeats of the microtubule-binding domain. Depending on the isoform incorporated in the fibril, tauopathies can be classified as 4R (CBD), 3R (FTD) or 4R/3R (AD). These different isoforms also have different conformations in each disease (Scheres et al., 2020) We imaged the purified fibrils with negative stain EM to confirm the typical disease-specific fibril shape (**Fig. 6C**). Both size and morphology can reveal information about fibril formation, interface and stability, correlating specifically with the disorder they are associated with. It is therefore of importance to characterise the size of various patient-derived fibrils as a means to differentiate Tau fibrils formed in different diseases and provide diagnosis.

We performed FIDA analysis to determine the size of the patient-derived Tau fibrils (**Fig. 6A**). The fibrils formed by recombinant TauRD had an average R_h of 54 nm. Fibrils measured from a patient diagnosed with AD had an apparent average R_h of 40 nm, with little variation between the measurements (**Fig 6A**). For CBD, the observed R_h was 140 nm (**Fig 6A**). Fibrils from FTD appeared to be a homogeneous population, with an average R_h of 60 nm (**Fig 6A**). These data reveal that FibrilPaint1 is suitable to interact with and characterise protein fibrils derived from primary material.

We then set out to calculate the average length of patient-derived fibrils from the R_h data and compared to the observed length in the single particle data. For comparing R_h values with actual fibril length, we generated a model to convert R_h

to fibril length. We stacked *in silico* layers on top each other and calculated the predicted size with FIDAbio R_h prediction tool. One full turn of the twist of a PHF comprises 342 layers (**Fig. 6D**). As the fibril structure is layer per layer 4.7 Å, full twist corresponds to a length of approximately 160 nm (Fitzpatrick et al., 2017). An R_h of 40 nm corresponds to a fibril of approximately 900 layers (**Fig. 6F**), which would give a fibril length of approximately 420 nm. To compare these values, we analysed the fibril population of negative staining EM data of AD sample. We assessed in total 103 fibrils, of which 48 showed a typical PHF structure (**Sup. Fig. 3**). We used the repetitive element in these fibrils to determine their average length. Averaging the length of the PHF fibrils revealed 2.7 turns, corresponding to 430 nm (**Fig. 6E**). This is consistent with the 420 nm observed in the FIDA experiments with the FibrilPaint1-stained fibrils. Thus, we conclude that combining FibrilPaint1 and FIDA is suitable to determine the length of pathological fibrils.

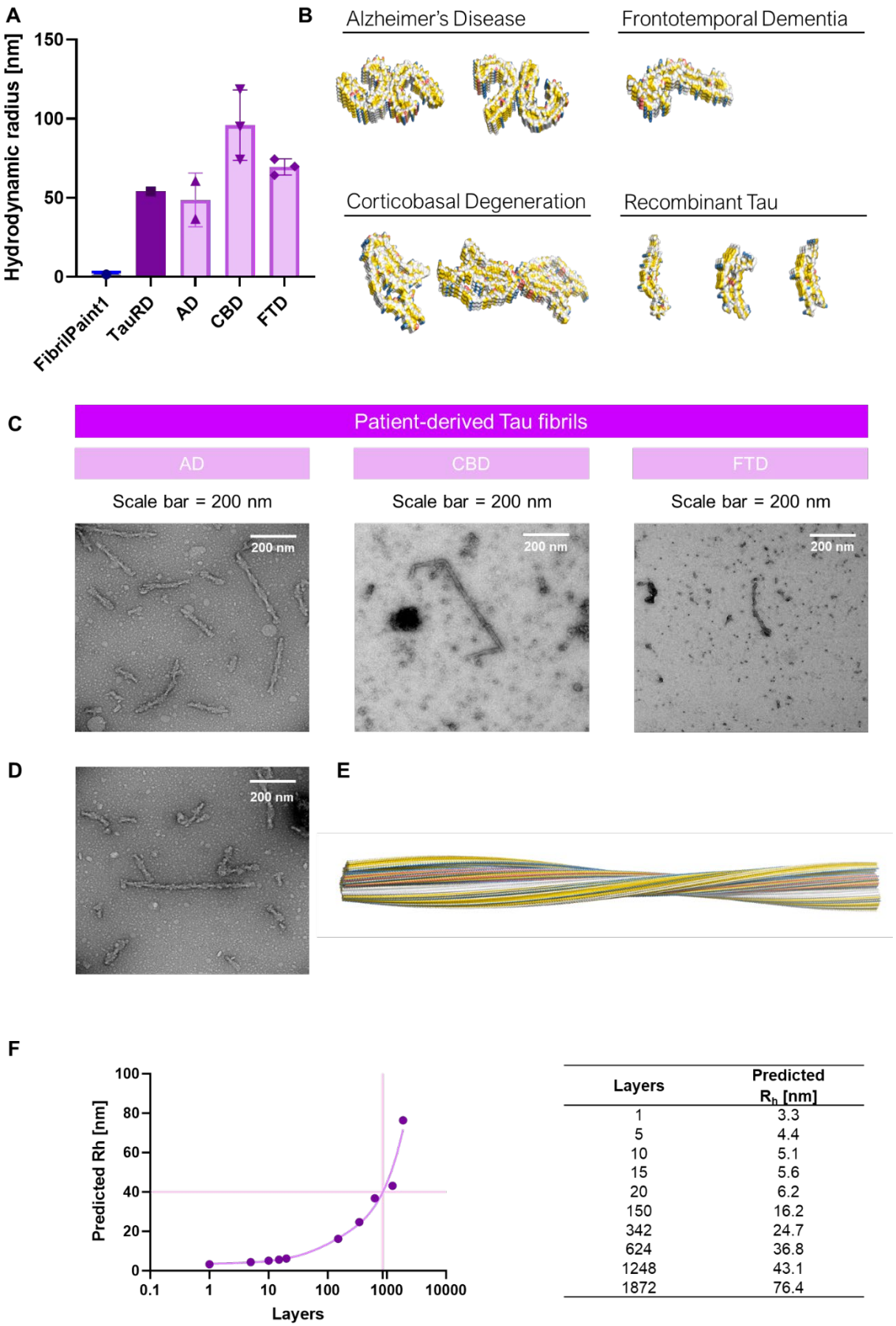

Layers	Predicted R_h [nm]
1	3.3
5	4.4
10	5.1
15	5.6
20	6.2
150	16.2
342	24.7
624	36.8
1248	43.1
1872	76.4

Figure 6 **Size assessment of patient-derived material from various tauopathies.** A) Hydrodynamic radius of fibrils extracted from patients diagnosed with Alzheimer's Diseases (AD), Frontotemporal Dementia (FTD) and Corticobasal Degeneration (CBD), measured with FibrilPaint1. (FibrilPaint1 only, blue; TauRD

fibrils, dark purple; fibrils retrieved from patients, light purple). B) Structural representation of the Tau fibrils of in different tauopathies, and recombinant Tau fibrils for comparison. The images were generated in PyMol software based on the coordinates of the cryo-EM structures. Functional groups are coloured according the YRB script. PDB codes: AD paired helical filament, 5O3L; AD straight filament, 5O3T; FTD narrow filament, 6GX5; CBD type I 6TJO; CBD type II 6VH7; Snake recombinant Tau, 6QJH; twister recombinant Tau, 6QJM; Jagged recombinant Tau 6QJP (Colours in YRB: hyrdophobic, yellow; negative charge, red; positive charge, blue). C) Negative stain EM of patient-derived fibrils from AD, CBD and FTD (FLTR). D) Example of AD fibrils designated in two groups: PHFs (blue) and fibrils that could not be clearly recognised as such (orange). E) Structural representation of AD paired helical filament consisting of 342 layers (left). The image was generated in PyMol software base of coordinates of cryo-EM structures. Functional groups are coloured according to YRB script. F) Hydrodynamic radius prediction of different layers of AD paired helical filament (left) using FIDAbio hydrodynamic radius prediction tool (right). Lines in prediction indicate the found average HR for AD fibrils, resembling 900 layers.

Discussion

We have developed FibrilPaint1, as a diagnostic tool that binds to amyloid fibrils but not their monomeric precursors. FibrilPaint1 is able to label patient-derived fibrils from three different tauopathies, which have different folds (Falcon et al., 2018; Fitzpatrick et al., 2017; Goedert et al., 2019; Scheres et al., 2020; Zhang et al., 2020). In combination with FIDA, FibrilPaint1 proves a valuable tool for the study of the aggregation pathway of TauRD and HttEx1Q44, two aggregating proteins which are unrelated in sequence and structure (**Fig. 1**). Importantly, FibrilPaint1 has a high specificity for amyloid fibrils, and does not recognize amorphous aggregates (**Fig. 3B**). FibrilPaint1 is therefore a specific tool accessible to determine the presence of fibrils, in all stages of the aggregation process.

FibrilPaint1 bypasses the need to label protein fibrils for modern fluorescence-based detection methods. FibrilPaint1 binds non-covalently to fibrils, without altering the structure of the fibrils (**Fig. 2, 5**). This proves useful when handling precious, patient-derived material, avoiding material loss or artefacts due to labelling procedures. It also allows the detection of amyloid fibrils in presence of cell lysate (**Fig. 3A).** FibrilPaint1 therefore proves to be a selective compound for detection of amyloids and can potentially be used as a tracer for detecting multiple aggregating diseases. With amyloidosis also present in other diseases such as diabetes, cardiomyopathy and Parkinson's Disease, FibrilPaint1 could be interesting tool for detecting pathological fibrils outside the brain such as the

liver, heart or guts respectively (Brundin et al., 2017; Cao et al., 2020; Ruberg et al., 2019).

The development of tracer diagnostics for early diagnosis of neurodegenerative diseases remains crucial. To date, Tauvid is the only FDA approved PET tracer for AD (Commissioner, 2020; Jie et al., 2021; Mohammadi et al., 2023). Cryo EM data reveals Tauvid does not bind in a regular stochiometric manner to AD fibrils, but it does to CTE Type I filaments (Shi et al., 2022). Regarding tracers for Htt, those have only been tested in *ex vivo* samples (Delva et al., 2022; Herrmann et al., 2021). Recently, fluid-based biomarkers emerged as novel diagnosis tools (Alcolea et al., 2023; Hansson et al., 2022; Teunissen et al., 2022). These markers provide valuable information about diagnosis, disease stage and progression. Moreover, fluid biomarkers are potentially more accessible and less expensive than PET tracers. We have demonstrated the ability of FibrilPaint1 to specifically bind to fibrils of patients diagnosed with AD, CBD and FTD (**Fig 6A**), as well as recombinant HttEx1Q44 fibrils (**Fig 2J**), at substoichiometric concentrations. This makes FibrilPaint1 a potential tracer specific to amyloid fibrils of varying nature, able to recognise the repetitive structure of the fibrils. The peptide-nature of FibrilPaint1 is biocompatible and can be further functionalised to develop a tracer for neurodegenerative diseases at early stages.

The combination of FibrilPaint1 with FIDA provides a valuable research tool. FibrilPaint1 with FIDA does not only establishes the presence of amyloids, but gives a structural parameter: R_h (Jensen & Østergaard, 2010). The average R_h of FibrilPaint1-stained fibrils is determined without bias towards larger or smaller particles, which could be useful to assess the stage of the disease (Lobanova, 2022; Nirmalraj et al., 2023). Also, with recent advances in cryo-EM, many fibril structures are available as PDB files (Scheres et al., 2020). The average R_h can then directly be associated with the structure of a fibril and hence with a specific disease to be diagnosed. Therefore, combining FibrilPaint1 with FIDA measurements allows to monitor the average length of the fibrils.

Remarkably, only FibrilPaint1 of our set of FibrilPaints can bind TauRD and HttEX1Q44 aggregates, while all were able to inhibit aggregation (**Fig. 2**).

Inhibition by FibrilPaints was also stronger on Huntingtin than our former peptide series (Garfagnini et al., 2022). The four peptides vary by an Arg or Asp in the beginning of the peptide and His or Thr at the end. Apparently, the binding mechanism is specific and dependent on these Arg and His combination of residues. Since FibrilPaint1 can bind two different aggregating species, the mechanism of binding must be related to recognition of the repetitive motif characteristic for amyloid fibrils (Gallardo et al., 2020; Iadanza et al., 2018) Both Arg and His are Nitrogen-Carbon π-stacking system, involving no oxygens. This enhances the π-stacking abilities generated by the Tryp in all FibrilPaints even further. We suspect that this is one of the most important properties of FibrilPaint1 for binding multiple aggregating species.

FibrilPaint1 is a suitable tool for further development into a tracer for neurodegenerative and other fibrillar diseases. The ability to specifically bind multiple amyloid fibrils opens the door for the diagnosis of varying neurodegenerative diseases. Its ability to recognize early aggregates provides the opportunity to recognize first stages of the diseases. This may allow intervention before severe damage in the brain has occurred.

Methods

Expression and purification of TauRD. We produced N-terminally FLAG-tagged (DYKDDDDK) human TauRD (Q244-E372, with pro-aggregation mutation ΔK280) in *E. Coli* BL21 Rosetta 2 (Novagen), with an additional removable N-terminal His_6-Smt-tag (MGHHHHHHGSDSEVNQEAKPEVKPEVKPETHINLKVSDGSSEIFFKIKKTTPL RRLMEAFAKRQGKEMDSLRFLYDGIRIQADQTPEDLDMEDNDIIEAHREQIGG). Expression was induced at OD_{600} 0.8 by addition of 0.15 mM IPTG and incubation at 18 °C overnight. Cells were harvested by centrifugation, resuspended in 25 mM HEPES-KOH pH=8.5, 50 mM KCl, flash frozen in liquid nitrogen, and kept at – 80 °C until further usage. Pellets were thawed at 37 °C, followed by the addition of ½ tablet/50 ml EDTA-free Protease Inhibitor and 5 mM β-mercaptoethanol. Cells were disrupted using an EmulsiFlex-C5 cell disruptor, and lysate was cleared by centrifugation. Supernatant was filtered using a 0.22 µm polypropylene filtered and purified with an ÄKTA purifier chromatography

System. Sample was loaded into a POROS 20MC affinity purification column with 50 mM HEPES-KOH pH 8.5, 50 mM KCl, eluted with a linear gradient 0-100%, 5 CV of 0.5 M imidazole. Fractions of interest were collected, concentrated to 2.5 ml using a buffer concentration column (vivaspin, MWCO 10 KDa), and desalted using PD-10 desalting column to HEPES pH 8.5, ½ tablet/50 ml Complete protease inhibitor, 5 mM β-mercaptoethanol. The His_6-Smt-tag was removed by treating the sample with Ulp1, 4 ^oC, shaking, overnight. The next day, sample was loaded into POROS 20HS column with HEPES pH 8.5, eluted with 0-100% linear gradient, 12 CV of 1M KCl. Fractions of interest were collected and loaded into a Superdex 26/60, 200 pg size exclusion column with 25 mM HEPES-KOH pH 7.5, 75 mM NaCl, 75 mM KCl. Fractions of interest were concentrated using a concentrator (vivaspin, MWCO 5 KDa) to desired concentration. Protein concentration was measured using a NanoDrop™ One^C UV/Vis spectrophotometer and purity was assessed by SDS-PAGE. Protein was aliquoted and stored at – 80 ^oC.

Expression and purification of HttEx1Q44. We produced HttEx1Q44 with in *E. Coli* BL21 Rosetta 2 (Novagen), with an additional N-terminal MBP- and C-terminal His_6-tag (MKIEEGKLVIWINGDKGYNGLAEVGKKFEKDTGIKVTVEHPDKLEEKFPQVAA
TGDGPDIIFWAHDRFGGYAQSGLLAEITPDKAFQDKLYPFTWDAVRYNGKLIA
YPIAVEALSLIYNKDLLPNPPKTWEEIPALDKELKAKGKSALMFNLQEPYFTWP
LIAADGGYAFKYENGKYDIKDVGVDNAGAKAGLTFLVDLIKNKHMNADTDYSIA
EAAFNKGETAMTINGPWAWSNIDTSKVNYGVTVLPTFKGQPSKPFVGVLSAGI
NAASPNKELAKEFLENYLLTDEGLEAVNKDKPLGAVALKSYEEELAKDPRIAAT
MENAQKGEIMPNIPQMSAFWYAVRTAVINAASGRQTVDAALAAAQTNAAAAS
EFSSNNNNNNNNNNLGIEGRMATLEKLMKAFESLKSFQQQQQQQQQQQQQ
QQQQQQQQQQQQQQQQQQQQQQQQQQQQQQQQQPPPPPPPPPPPQLPQP
PPQAQPLLPQPQPPPPPPPPPPGPAVAEEPLHRPSGSHHHHHH). We induced expression at an OD_{600} of 0.8 by adding 0.15 mM IPTG and incubating at 18 ^oC overnight. Cells were harvested by centrifugation and resuspended in 50 mM HEPES-KOH pH=8.5, 50 mM KCl with ½ tablet/50 ml EDTA-free Protease Inhibitor and 5 mM β-mercaptoethanol. Cells were disrupted using an EmulsiFlex-C5 cell disruptor, and lysate was cleared by centrifugation. Supernatant was

filtered using a 0.22 µm polypropylene filtered and purified with an ÄKTA purifier chromatography System. Sample was loaded into a POROS 20MC affinity purification column with 50 mM HEPES-KOH pH 8.5, 100 mM KCl, eluted with a linear gradient 0-100%, 10 CV of 0.5 M imidazole, 30 mM NaCl. Fractions of interest were collected and concentrated to desired concentration using concentrating column (vivaspin, MWCO 30 KDa). Protein concentration was measured using a NanoDrop™ One^{C} UV/Vis spectrophotometer and purity was assessed by SDS-PAGE. Protein was aliquoted and stored at – 80 ºC.

Peptide synthesis and purification

The peptides were synthesized using a Liberty Blue Microwave-Assisted Peptide Synthesizer (CEM) with standard Fmoc chemistry and Oxyma/DIC as coupling reagents. The peptide concentrations were measured by UV spectroscopy. The peptides were labeled with 5(6)-carboxyfluorescein at their N' termini. The peptides were cleaved from the resin with a mixture of 95% (v/v) trifluoroacetic acid (TFA), 2.5% (v/v) triisopropylsilane (TIS), 2.5% (v/v) triple distilled water (TDW) agitating vigorously for 3 hours at room temperature. The volume was decreased by N_2 flux and the peptides precipitated by addition of 4 volumes of diethylether at -20 °C. The peptides were sedimented at -20 °C for 30 minutes, then centrifuged and the diethylether discarded. The peptides were washed three times with diethylether and dried by gentle N_2 flux. The solid was dissolved in 1:2 volume ratio of acetonitrile ACN:TDW, frozen in liquid Nitrogen and lyophilized. The peptides were purified on a WATERS HPLC using a reverse-phase C18 preparative column with a gradient of ACN/TDW. The identity and purity of the peptides was verified by ESI mass spectrometry and Merck Hitachi analytical HPLC using a reverse-phase C8 analytical column.

Fibril extraction

Brain material of FTD and CBD were obtained from the Dutch Brain Bank, project number 1369. Brain material for AD was donated by prof. J. J. M. Hoozemans from the VU Medical Centra Amsterdam.

PHFs and SFs were extracted from grey matter of prefrontal cortex from patients diagnosed with AD. Tissue was homogenized using a Polytron(PT 2500E, Kinematica AG) on max speed in 20 % (w/v) A68 buffer, consisting of 20 mM

TRIS-HCl pH 7.4, 10 mM EDTA, 1.6 M NaCl, 10% sucrose, 1 tablet/10 ml Pierce protease inhibitor, 1 tablet/10 ml phosphatase inhibitor. The homogenized sample was spun from 20 minutes, at 14000 rpm at 4 ºC. Supernatant was collected, and the pellet was homogenized in 10% (w/v) A68 buffer. The homogenized was spun once more. The supernatants of both centrifugations were combined and supplied with 10% w/v Sarkosyl, and incubated for 1 hour on a rocker at room temperature. The sample was ultracentrifuged for 1 hour at 100000xg and 4 ºC. The supernatant was discarded, and the pellet was incubated overnight at 4 ºC in 20 µl/0.2 g starting material of 50 mM TRIS-HCl pH 7.4. The next day, the pellet was diluted up to 1 ml of A68 buffer, and resuspended. To get rid of contamination, the sample was spun for 30 minutes at 14000 rpm, 4 ºC. Supernatant was collected and spun once more for 1 hour at 100000xg, 4 ºC. The pellet was resuspended in 30 µl 25 mM HEPES-KOH pH 7.4, 75 mM KCl, 75 mM NaCl, and stored at 4 ºC up to a month.

Narrow filaments were extracted from the grey matter of the middle frontal gyrus from patients diagnosed with FTD. Fibrils were extracted following the protocol for AD fibrils. After the first ultracentrifugation step, the pellet was resuspended in 250 µl/1g of starting material of 50 mM Tris pH 7.5, 150 mM NaCl, 0.02% amphipol A8-35. The sample was centrifuged for 30 minutes at 3000xg and 4 ºC. Pellet was discarded, and the supernatant was ultracentrifuged for 1 hour at 100000xg and 4 ºC. The pellet was resuspended in 30 µl of 50 mM TRIS-HCl pH 7.4, 150 mM NaCl, and stored at 4 ºC up to a month.

CBD fibrils were extracted from the grey matter of the superior parietal gyrus of patients diagnosed with CBD. Tissue was homogenized using a Polytron(PT 2500E, Kinematica AG) on max speed in 20 % w/v 10 mM TRIS-HCl pH 7.5, 1 mM EGTA, 0.8 M NaCl, 10% sucrose. The homogenate was supplied with 2% w/v of sarkosyl and incubated for 20 minutes at 37 ºC. The sample was centrifuged for 10 minutes at 20000xg, and 25 ºC. The supernatant was ultracentrifuged for 20 minutes at 100000xg and 25 ºC. The pellet was resuspended in 750 µl/1g starting material of 10 mM TRIS-HCl pH 7.5, 1 mM EGTA, 0.8 M NaCl, 10% sucrose, and centrifuged at 9800xg for 20 minutes. The supernatant was ultracentrifuged for 1 hour at 100000xg. The pellet was

resuspended in 25 µl/g starting material of 20 mM TRIS-HCl pH 7.4, 100 mM NaCl, and stored at 4 ºC up to a month.

ThioflavinT aggregation assay

Aggregation of 20 µM Tau-RD in 25 mM HEPES-KOH pH 7.4, 75 mM KCl, 75 mM NaCl, ½ tablet/50 ml Protease Inhibitor, was induced by the addition 5 µM of heparin low molecular weight in presence of 45 µM ThioflavinT. Impact of peptides was assessed by adding 0.02, 0.2 or 2 µM of peptide. Fluorescent spectra was recorder every 5 minutes, at 37 ºC and 600 rpm during 24 hours in CLARIOstar® Plus.

Aggregation of 20 µM HttEx1Q44 in 25 mM HEPES-KOH pH 7.4, 75 mM KCl, 75 mM NaCl, ½ tablet/50 ml Protease Inhibitor, was induced by the cleavage of C-terminal MBP-tag with Factor Xa, in presence of 45 µM ThioflavinT. Impact of peptides was assessed by adding 0.02, 0.2 or 2 µM of peptide. Fluorescent spectra was recorder every 5 minutes, at 37 ºC and 600 rpm during 24 hours in CLARIOstar® Plus.

Negative Staining Electron Microscopy (nsEM)

Fibril samples were diluted to concentrations between 2 µM and 20 µM, and stored in an ice bath until preparation of grids at room temperature. Copper grids with continuous carbon were glow discharged in air of 0.1 bar for 15 sec, using a current of 10 mA, before applying a sample volume of 2.0 µL that was allowed to incubate on the carbon for 60 sec. After incubation, the grid was blotted and subsequently washed twice in 4 µL of milli-Q water and stained twice in 4 µL of uranyl acetate (2w/v% in water), making sure to blot it dry before proceeding to the next droplet. The second droplet of uranyl acetate was left to incubate for 60 sec on the grid, after which it was blotted nearly entirely and left to evaporate for 5 minutes. Imaging took place on a Talos L120C transmission electron microscope from Thermo Fisher Scientific, operating at 120 kV in micro-probe mode. Using a defocus between -1.0 µm and -2.0 µm, the CETA camera recorded images at magnifications of 210, 1.250, 11.000, 36.000, 57.000, and 120.000x, corresponding to an approximate dose between 1 e/A2 and 50 e/A2 depending on the exact magnification.

Size measurement with Flow Induced Dispersion Analysis (FIDA)

Flow Induced Dispersion Analysis (FIDA) was used to determine fibril size. The FIDA experiments were performed using a FIDA1 with a 480 nm excitation source.

Different timepoint preformed Tau-RD or HttEx1Q44 fibrils were diluted to a final concentration of 2 µM (calculated as if monomer concentration) in 25 mM HEPES-KOH pH 7.5, 75 mM KCl, 75 mM NaCl, 0.5% pluronic (for Tau-RD) or 50 mM HEPES-KOH pH 7.5, 150 mM KCl, 0.5% pluronic (for HttExQ4), together with 200 nM of FibrilPaint1. For patient derived Tau filaments, AD, CBD or FTD fibrils were diluted to a final concentration of 2 µM in 20 mM TRIS-HCl pH 7.4, 100 mM NaCl, 0.5 % pluronic (for AD and CBD), or 50 mM TRIS-HCl pH 7.4, 150 mM NaCl, 0.5 % pluronic (for FTD). The mode of operation use is capillary dissociation (Capdis). In this, the capillary is equilibrated with buffer followed by injection of the sample. Only the indicator sample contains fibrils, in order to minimize stickiness to the capillary.

Table 3 Experimental parameters for Capdis analysis of protein fibril size up to a R_h of 75 nm.

Tray	Vial	Pressure (mbar)	Time (s)	Outlet	Measure	Comments
2	1	3500	45	Variable	No	1 M NaOH
2	2	3500	75	Variable	No	Buffer equilibration
1	Analyte	3500	20	Variable	No	Buffer
1	Indicator	50	10	Variable	No	Sample application
1	Analyte	75	1800	Variable	Yes	Buffer
Tray 1 was maintained at 37 ºC and tray 2 and capillary chamber at 25 ºC						

Table 4 Experimental parameters for Capdis analysis of protein fibrils size of R_h 75-150 nm.

Tray	Vial	Pressure (mbar)	Time (s)	Outlet	Measure	Comments
2	1	3500	45	Variable	No	1 M NaOH
2	2	3500	75	Variable	No	Buffer equilibration

1	Analyte	3500	20	Variable	No	Buffer
1	Indicator	50	10	Variable	No	Sample application
1	Analyte	30	5000	Variable	Yes	Buffer
Tray 1 was maintained at 37 ºC and tray 2 and capillary chamber at 25 ºC						

Table 5 Experimental parameters for Capdis analysis of protein fibrils size of R_h 150 nm and larger.

Tray	Vial	Pressure (mbar)	Time (s)	Outlet	Measure	Comments
2	1	3500	45	Variable	No	1 M NaOH
2	2	3500	75	Variable	No	Buffer equilibration
1	Analyte	3500	20	Variable	No	Buffer
1	Indicator	50	10	Variable	No	Sample application
1	Analyte	30	5000	Variable	Yes	Buffer
Tray 1 was maintained at 37 ºC and tray 2 and capillary chamber at 25 ºC						

Calculation of fibril length from R_h

For a perfectly spherical particle, the R_h is identical to the radius of the sphere. For fibrils, the shape can be approximated as a cylinder. When the length is at least five times as big as the radius (L/R>5), we can apply the Equation 1 (He & Niemeyer, 2003; Yoshizaki & Yamakawa, 1980):

Equation 1:

$$L = 2\ R_h\, S$$

$$s = \ln\left(\frac{L}{R} + \left(\frac{L^2}{R^2} + 1\right)^{\frac{1}{2}}\right) - \frac{R}{L}\left(\frac{L^2}{R^2} + 1\right)^{\frac{1}{2}} + \frac{R}{L}$$

Using equation 1, where L is the length and R the radius of the analysed particle, we have created a graph to help estimate the fibril length of the measured species (**Sup. Fig. 1**)

Acknowledgements

We thank the Protein Research Centre of Utrecht University for access to instrumentation. SGDR was supported by grants of the Campaign Team Huntington and Alzheimer Nederland (No. WE.03-2019-03) and a ZonMW TOP grant (No. 91215084). AF thanks The Minerva Center for Bio-Hybrid complex systems and the Saerree K. and Louis P. Fiedler Chair in Chemistry.

Conflict of interest

JAP, FAD, TG, GM, AF and SGDR are named as inventors in a patent (EP23194706, 'Peptides for the detection of amyloid fibril Aggregates') filed by Universiteit Utrecht Holding BV describing the peptides mentioned in this manuscript. HJ is the C.S.O. of FIDA Biosystems. The other authors declare no competing interests.

Author contributions

Conception JAP, FAD, TG, GM, AF, SGDR
Design of the work JAP, FAD, SGDR
Acquisition JAP, FAD, MBK, MB, JJMH
Analysis JAP, FAD, HJ, AF, SGDR
Interpretation of data JAP, FAD, HJ, AF, SGDR
Writing original draft JAP, FAD
Revision JAP, FAD, MBK, HJ, TG, JJHM, FF, AF and SGDR

References

Alcolea, D., Beeri, M. S., Rojas, J. C., Gardner, R. C., & Lleó, A. (2023). Blood Biomarkers in Neurodegenerative Diseases. *Neurology*, *101*(4), 172-180. https://doi.org/10.1212/wnl.0000000000207193

Andrew, S. E., Goldberg, Y. P., Kremer, B., Telenius, H., Theilmann, J., Adam, S., Starr, E., Squitieri, F., Lin, B., & Kalchman, M. A. (1993). The relationship between trinucleotide (CAG) repeat length and clinical features of Huntington's disease. *Nature genetics*, *4*(4), 398-403. https://doi.org/10.1038/ng0893-398

Arendt, T., Stieler, J. T., & Holzer, M. (2016). Tau and tauopathies. *Brain research bulletin*, *126*(Pt 3), 238-292. https://doi.org/S0361-9230(16)30232-5 [pii]

Association, A. s. (2016). 2016 Alzheimer's disease facts and figures. *Alzheimer's & Dementia*, *12*(4), 459-509. https://doi.org/10.1016/j.jalz.2016.03.001

Ballatore, C., Lee, V. M., & Trojanowski, J. Q. (2007). Tau-mediated neurodegeneration in Alzheimer's disease and related disorders. *Nature reviews.Neuroscience*, *8*(9), 663-672. https://doi.org/nrn2194 [pii]

Bejanin, A., Schonhaut, D. R., La Joie, R., Kramer, J. H., Baker, S. L., Sosa, N., Ayakta, N., Cantwell, A., Janabi, M., Lauriola, M., O'Neil, J. P., Gorno-Tempini, M. L., Miller, Z. A., Rosen, H. J., Miller, B. L., Jagust, W. J., & Rabinovici, G. D. (2017). Tau pathology and neurodegeneration contribute to cognitive impairment in Alzheimer's disease. *Brain : a journal of neurology*, *140*(12), 3286-3300. https://doi.org/10.1093/brain/awx243

Boatz, J. C., Piretra, T., Lasorsa, A., Matlahov, I., Conway, J. F., & van der Wel, P. C. A. (2020). Protofilament Structure and Supramolecular Polymorphism of Aggregated Mutant Huntingtin Exon 1. *Journal of Molecular Biology*, *432*(16), 4722-4744. https://doi.org/S0022-2836(20)30418-6 [pii]

Bradford, A., Kunik, M. E., Schulz, P., Williams, S. P., & Singh, H. (2009). Missed and Delayed Diagnosis of Dementia in Primary Care. *Alzheimer Disease & Associated Disorders*, *23*(4), 306-314. https://doi.org/10.1097/wad.0b013e3181a6bebc

Brundin, P., Dave, K. D., & Kordower, J. H. (2017). Therapeutic approaches to target alpha-synuclein pathology. *Experimental neurology*, *298*, 225-235. https://doi.org/https://doi.org/10.1016/j.expneurol.2017.10.003

Cao, Q., Boyer, D. R., Sawaya, M. R., Ge, P., & Eisenberg, D. S. (2020). Cryo-EM structure and inhibitor design of human IAPP (amylin) fibrils. *Nature Structural & Molecular Biology*, *27*(7), 653-659. https://doi.org/10.1038/s41594-020-0435-3

Commissioner, O. o. t. (2020). FDA Approves First Drug to Image Tau Pathology in Patients Being Evaluated for Alzheimer’s Disease. In (Vol. 2023): FDA.

Conti, E., Franks, N. P., & Brick, P. (1996). Crystal structure of firefly luciferase throws light on a superfamily of adenylate-forming enzymes. *Structure (London, England : 1993)*, *4*(3), 287-298. https://doi.org/10.1016/s0969-2126(96)00033-0

Day, G. S., Scarmeas, N., Dubinsky, R., Coerver, K., Mostacero, A., West, B., Wessels, S. R., & Armstrong, M. J. (2022). Aducanumab Use in Symptomatic Alzheimer Disease Evidence in Focus. *Neurology*, *98*(15), 619-631. https://doi.org/10.1212/wnl.0000000000200176

Delva, A., Koole, M., Serdons, K., Bormans, G., Liu, L., Bard, J., Khetarpal, V., Dominguez, C., Munoz-Sanjuan, I., Wood, A., Skinbjerg, M., Wang, Y., Vandenberghe, W., & Van Laere, K. (2022). Biodistribution and dosimetry in human healthy volunteers of the PET radioligands [(11)C]CHDI-00485180-R and [(11)C]CHDI-00485626, designed for quantification of cerebral aggregated mutant huntingtin. *European journal of nuclear medicine and molecular imaging*, *50*(1), 48-60. https://doi.org/10.1007/s00259-022-05945-z

Elena-Real, C. A., Sagar, A., Urbanek, A., Popovic, M., Morató, A., Estaña, A., Fournet, A., Doucet, C., Lund, X. L., Shi, Z.-D., Costa, L., Thureau, A., Allemand, F., Swenson, R. E., Milhiet, P.-E., Crehuet, R., Barducci, A., Cortés, J., Sinnaeve, D., . . . Bernadó, P. (2023). The structure of pathogenic huntingtin exon 1 defines the bases of its aggregation propensity. *Nature Structural & Molecular Biology*, *30*(3), 309-320. https://doi.org/10.1038/s41594-023-00920-0

Elghetany, M. T., & Saleem, A. (1988). Methods for staining amyloid in tissues: a review. *Stain technology*, *63*(4), 201-212. https://doi.org/10.3109/10520298809107185

Falcon, B., Zhang, W., Murzin, A. G., Murshudov, G., Garringer, H. J., Vidal, R., Crowther, R. A., Ghetti, B., Scheres, S. H. W., & Goedert, M. (2018). Structures of filaments from Pick's disease reveal a novel tau protein fold. *Nature*, *561*(7721), 137-140. https://doi.org/10.1038/s41586-018-0454-y

Falcon, B., Zivanov, J., Zhang, W., Murzin, A. G., Garringer, H. J., Vidal, R., Crowther, R. A., Newell, K. L., Ghetti, B., Goedert, M., & Scheres, S. H. W. (2019). Novel tau filament fold in chronic traumatic encephalopathy encloses hydrophobic molecules. *Nature*, *568*(7752), 420-423. https://doi.org/10.1038/s41586-019-1026-5

Ferrari, L., Stucchi, R., Konstantoulea, K., van de Kamp, G., Kos, R., Geerts, W. J. C., van Bezouwen, L. S., Förster, F. G., Altelaar, M., Hoogenraad, C. C., & Rüdiger, S. G. D. (2020). Arginine pi-stacking drives binding to fibrils of the Alzheimer protein Tau. *Nature communications*, *11*(1), 571-577. https://doi.org/10.1038/s41467-019-13745-7

Fitzpatrick, A. W. P., Falcon, B., He, S., Murzin, A. G., Murshudov, G., Garringer, H. J., Crowther, R. A., Ghetti, B., Goedert, M., & Scheres, S. H. W. (2017). Cryo-EM structures of tau filaments from Alzheimer's disease. *Nature*, *547*(7662), 185-190. https://doi.org/10.1038/nature23002

Gallardo, R., Ranson, N. A., & Radford, S. E. (2020). Amyloid structures: much more than just a cross-β fold. *Current Opinion in Structural Biology*, *60*, 7-16. https://doi.org/S0959-440X(19)30102-2 [pii]

Garfagnini, T., Ferrari, L., Koopman, M. B., Halters, S., Van Kappel, E., Mayer, G., Maurice, M. M., Rüdiger, S. G. D., & Friedler, A. (2022). A peptide strategy for inhibiting different protein aggregation pathways in disease. *bioRxiv*, 2022.2010.2022.513060. https://doi.org/10.1101/2022.10.22.513060

Goedert, M., Falcon, B., Zhang, W., Ghetti, B., & Scheres, S. H. W. (2019). Distinct Conformers of Assembled Tau in Alzheimer's and Pick's Diseases. *Cold Spring Harbor symposia on quantitative biology*. https://doi.org/037580 [pii]

Hagemans, D., van Belzen, I. A. M., Morán Luengo, T., & Rüdiger, S. G. D. (2015). A script to highlight hydrophobicity and charge on protein surfaces. *Frontiers in molecular biosciences*, *2*, 56. https://doi.org/10.3389/fmolb.2015.00056

Hansson, O., Edelmayer, R. M., Boxer, A. L., Carrillo, M. C., Mielke, M. M., Rabinovici, G. D., Salloway, S., Sperling, R., Zetterberg, H., & Teunissen, C. E. (2022). The Alzheimer's Association appropriate use recommendations for blood biomarkers in Alzheimer's disease. *Alzheimer's & Dementia*, *18*(12), 2669-2686. https://doi.org/10.1002/alz.12756

He, L. Z., & Niemeyer, B. (2003). A Novel Correlation for Protein Diffusion Coefficients Based on Molecular Weight and Radius of Gyration. *Biotechnology Progress*, *19*(2), 544-548. https://doi.org/10.1021/bp0256059

Helabad, B. M., Matlahov, I., Daldrop, J. O., Jain, G., van der Wel, P. C. A., & Miettinen, M. S. (2023). Integrative determination of the atomic structure of mutant huntingtin exon 1 fibrils from Huntington's disease. *bioRxiv*. https://doi.org/10.1101/2023.07.21.549993

Herrmann, F., Hessmann, M., Schaertl, S., Berg-Rosseburg, K., Brown, C. J., Bursow, G., Chiki, A., Ebneth, A., Gehrmann, M., Hoeschen, N., Hotze, M., Jahn, S., Johnson, P. D., Khetarpal, V., Kiselyov, A., Kottig, K., Ladewig, S., Lashuel, H., Letschert, S., . . . Bard, J. A. (2021). Pharmacological characterization of mutant huntingtin aggregate-directed PET imaging

tracer candidates. *Scientific Reports*, *11*(1), 17977. https://doi.org/10.1038/s41598-021-97334-z

Howie, A. J., Brewer, D. B., Howell, D., & Jones, A. P. (2008). Physical basis of colors seen in Congo red-stained amyloid in polarized light. *Laboratory investigation; a journal of technical methods and pathology*, *88*(3), 232-242. https://doi.org/10.1038/labinvest.3700714

Iaccarino, L., La Joie, R., Edwards, L., Strom, A., Schonhaut, D. R., Ossenkoppele, R., Pham, J., Mellinger, T., Janabi, M., Baker, S. L., Soleimani-Meigooni, D., Rosen, H. J., Miller, B. L., Jagust, W. J., & Rabinovici, G. D. (2021). Spatial Relationships between Molecular Pathology and Neurodegeneration in the Alzheimer's Disease Continuum. *Cerebral cortex (New York, N.Y.: 1991)*, *31*(1), 1-14. https://doi.org/10.1093/cercor/bhaa184

Iadanza, M. G., Jackson, M. P., Hewitt, E. W., Ranson, N. A., & Radford, S. E. (2018). A new era for understanding amyloid structures and disease. *Nature Reviews Molecular Cell Biology*, *19*(12), 755-773. https://doi.org/10.1038/s41580-018-0060-8

Isas, J. M., Langen, A., Isas, M. C., Pandey, N. K., & Siemer, A. B. (2017). Formation and Structure of Wild Type Huntingtin Exon-1 Fibrils. *Biochemistry*, *56*(28), 3579-3586. https://doi.org/10.1021/acs.biochem.7b00138

Isas, M. J., Pandey, N. K., Xu, H., Teranishi, K., Okada, A. K., Fultz, E. K., Rawat, A., Applebaum, A., Meier, F., Chen, J., Langen, R., & Siemer, A. B. (2021). Huntingtin fibrils with different toxicity, structure, and seeding potential can be interconverted. *Nature communications*, *12*(1). https://doi.org/10.1038/s41467-021-24411-2

Jack, C. R., Wiste, H. J., Botha, H., Weigand, S. D., Therneau, T. M., Knopman, D. S., Graff-Radford, J., Jones, D. T., Ferman, T. J., Boeve, B. F., Kantarci, K., Lowe, V. J., Vemuri, P., Mielke, M. M., Fields, J. A., Machulda, M. M., Schwarz, C. G., Senjem, M. L., Gunter, J. L., & Petersen, R. C. (2019). The bivariate distribution of amyloid-? and tau: relationship with established neurocognitive clinical syndromes. *Brain : a journal of neurology*, *142*(10), 3230-3242. https://doi.org/10.1093/brain/awz268

Jensen, H., & Østergaard, J. (2010). Flow induced dispersion analysis quantifies noncovalent interactions in nanoliter samples. *Journal of the American Chemical Society*, *132*(12), 4070-4071. https://doi.org/10.1021/ja100484d

Jie, C. V. M. L., Treyer, V., Schibli, R., & Mu, L. (2021). Tauvid™: The First FDA-Approved PET Tracer for Imaging Tau Pathology in Alzheimer's Disease. *Pharmaceuticals (Basel, Switzerland)*, *14*(2), 110. https://doi.org/10.3390/ph14020110

Ko, J., Ou S Fau - Patterson, P. H., & Patterson, P. H. (2001). New anti-huntingtin monoclonal antibodies: implications for huntingtin conformation and its binding proteins. *Brain research bulletin*(0361-9230 (Print)).

Ksiezak-Reding, H., Dickson, D. W., Davies, P., & Yen, S. H. (1987). Recognition of tau epitopes by anti-neurofilament antibodies that bind to Alzheimer neurofibrillary tangles. *Proceedings of the National Academy of Sciences of the United States of America*, *84*(10), 3410-3414. https://doi.org/10.1073/pnas.84.10.3410

Leuzy, A., Smith, R., Ossenkoppele, R., Santillo, A., Borroni, E., Klein, G., Ohlsson, T., J?gi, J., Palmqvist, S., Mattsson-Carlgren, N., Strandberg, O., Stomrud, E., & Hansson, O. (2020). Diagnostic Performance of RO948 F 18 Tau Positron Emission Tomography in the Differentiation of Alzheimer Disease From Other Neurodegenerative Disorders. *JAMA neurology*, *77*(8), 955-965. https://doi.org/10.1001/jamaneurol.2020.0989

Lieberman, A. P., Shakkottai, V. G., & Albin, R. L. (2019). Polyglutamine Repeats in Neurodegenerative Diseases. *Annual Review of Pathology: Mechanisms of Disease*, *14*(1), 1-27. https://doi.org/10.1146/annurev-pathmechdis-012418-012857

Liu, L., Johnson, P. D., Prime, M. E., Khetarpal, V., Lee, M. R., Brown, C. J., Chen, X., Clark-Frew, D., Coe, S., Conlon, M., Davis, R., Ensor, S., Esposito, S., Moren, A. F., Gai, X., Green, S., Greenaway, C., Haber, J., Halldin, C., . . . Dominguez, C. (2021). (11)C]CHDI-626, a PET Tracer Candidate for Imaging Mutant Huntingtin Aggregates with Reduced Binding to

AD Pathological Proteins. *Journal of medicinal chemistry*, *64*(16), 12003-12021. https://doi.org/10.1021/acs.jmedchem.1c00667

Liu, L., Prime, M. E., Lee, M. R., Khetarpal, V., Brown, C. J., Johnson, P. D., Miranda-Azpiazu, P., Chen, X., Clark-Frew, D., Coe, S., Davis, R., Dickie, A., Ebneth, A., Esposito, S., Gadouleau, E., Gai, X., Galan, S., Green, S., Greenaway, C., . . . Dominguez, C. (2020). Imaging Mutant Huntingtin Aggregates: Development of a Potential PET Ligand. *Journal of medicinal chemistry*, *63*(15), 8608-8633. https://doi.org/10.1021/acs.jmedchem.0c00955

Lobanova, E., Whiten, D., Ruggeri, F. S., Taylor, C. G., Kouli, A., Xia, Z., Emin, D., Zhang, Y. P., L Lam, J. Y., Williams-Gray, C. H., Klenerman, D. (2022). Imaging protein aggregates in the serum and cerebrospinal fluid in Parkinson's disease. *Brain : a journal of neurology*(145(2)), 632-643. https://doi.org/https://doi.org/10.1093/brain/awab306

Long, S., Benoist, C., & Weidner, W. (2023). *World Alzheimer Report 2023: Reducing dementia risk: never too early, never too late*.

Martí-Martínez, S., & Valor, L. M. (2022). A Glimpse of Molecular Biomarkers in Huntington's Disease. *International journal of molecular sciences*, *23*(10), 5411. https://doi.org/10.3390/ijms23105411

Matlahov, I., Boatz, J. C., & van der Wel, P. C. A. (2022). Selective observation of semi-rigid non-core residues in dynamically complex mutant huntingtin protein fibrils. *Journal of structural biology: X*, *6*, 100077. https://doi.org/10.1016/j.yjsbx.2022.100077

Merz, G. E., Chalkley, M. J., Tan, S. K., Tse, E., Lee, J., Prusiner, S. B., Paras, N. A., Degrado, W. F., & Southworth, D. R. (2023). Stacked binding of a PET ligand to Alzheimer's tau paired helical filaments. *Nature communications*, *14*(1). https://doi.org/10.1038/s41467-023-38537-y

Miller, C. C. (1924). The Stokes-Einstein law for diffusion in solution. *Proceedings of the Royal Society of London. Series A, Containing Papers of a Mathematical and Physical Character*, *106*(740), 724-749. https://doi.org/10.1098/rspa.1924.0100

Mohammadi, Z., Alizadeh, H., Marton, J., & Cumming, P. (2023). The Sensitivity of Tau Tracers for the Discrimination of Alzheimer's Disease Patients and Healthy Controls by PET. *Biomolecules*, *13*(2), 290. https://doi.org/10.3390/biom13020290

Mueller, A., Bullich, S., Barret, O., Madonia, J., Berndt, M., Papin, C., Perrotin, A., Koglin, N., Kroth, H., Pfeifer, A., Tamagnan, G., Seibyl, J. P., Marek, K., De Santi, S., Dinkelborg, L. M., & Stephens, A. W. (2020). Tau PET imaging with ¹⁸F-PI-2620 in Patients with Alzheimer Disease and Healthy Controls: A First-in-Humans Study. *Journal of Nuclear Medicine*, *61*(6), 911-919. https://doi.org/10.2967/jnumed.119.236224

Nazarov, S., Chiki, A., Boudeffa, D., & Lashuel, H. A. (2022). Structural Basis of Huntingtin Fibril Polymorphism Revealed by Cryogenic Electron Microscopy of Exon 1 HTT Fibrils. *Journal of the American Chemical Society*, *144*(24), 10723-10735. https://doi.org/10.1021/jacs.2c00509

Nirmalraj, P. N., Schneider, T., Lüder, L., & Felbecker, A. (2023). Protein fibril length in cerebrospinal fluid is increased in Alzheimer's disease. *Communications biology*, *6*(1). https://doi.org/10.1038/s42003-023-04606-7

Organization, W. H. (2017). *Global action plan on the public health response to dementia 2017-2025*.

Ossenkoppele, R., & Hansson, O. (2021). Towards clinical application of tau PET tracers for diagnosing dementia due to Alzheimer's disease. *Alzheimer's & Dementia*, *17*(12), 1998-2008. https://doi.org/10.1002/alz.12356

Ossenkoppele, R., Rabinovici, G. D., Smith, R., Cho, H., Sch□ll, M., Strandberg, O., Palmqvist, S., Mattsson, N., Janelidze, S., Santillo, A., Ohlsson, T., J□gi, J., Tsai, R., La Joie, R., Kramer, J., Boxer, A. L., Gorno-Tempini, M. L., Miller, B. L., Choi, J. Y., . . . Hansson, O. (2018). Discriminative Accuracy of [18F]flortaucipir Positron Emission Tomography for

Alzheimer Disease vs Other Neurodegenerative Disorders. *Jama*, *320*(11), 1151-1162. https://doi.org/10.1001/jama.2018.12917

Ossenkoppele, R., Schonhaut, D. R., Schöll, M., Lockhart, S. N., Ayakta, N., Baker, S. L., O'Neil, J. P., Janabi, M., Lazaris, A., Cantwell, A., Vogel, J., Santos, M., Miller, Z. A., Bettcher, B. M., Vossel, K. A., Kramer, J. H., Gorno-Tempini, M. L., Miller, B. L., Jagust, W. J., & Rabinovici, G. D. (2016). Tau PET patterns mirror clinical and neuroanatomical variability in Alzheimer's disease. *Brain : a journal of neurology*, *139*(Pt 5), 1551-1567. https://doi.org/10.1093/brain/aww027

Palmqvist, S., Mattsson, N., & Hansson, O. (2016). Cerebrospinal fluid analysis detects cerebral amyloid-β accumulation earlier than positron emission tomography. *Brain*, *139*(Pt 4), 1226-1236. https://doi.org/10.1093/brain/aww015

Parsell, D. A., Kowal, A. S., Singer, M. A., & Lindquist, S. (1994). Protein disaggregation mediated by heat-shock protein Hsp104. *Nature*, *372*(6505), 475-478. https://doi.org/10.1038/372475a0

Ruberg, F. L., Grogan, M., Hanna, M., Kelly, J. W., & Maurer, M. S. (2019). Transthyretin Amyloid Cardiomyopathy: JACC State-of-the-Art Review. *J Am Coll Cardiol*, *73*(22), 2872-2891. https://doi.org/10.1016/j.jacc.2019.04.003

Saudou, F., & Humbert, S. (2016). The Biology of Huntingtin. *Neuron*, *89*(5), 910-926. https://doi.org/10.1016/j.neuron.2016.02.003

Scheres, S. H., Zhang, W., Falcon, B., & Goedert, M. (2020). Cryo-EM structures of tau filaments. *Current Opinion in Structural Biology*, *64*, 17-25. https://doi.org/S0959-440X(20)30082-8 [pii]

Scheufler, C., Brinker, A., Bourenkov, G., Pegoraro, S., Moroder, L., Bartunik, H., Hartl, F. U., & Moarefi, I. (2000). Structure of TPR domain-peptide complexes: critical elements in the assembly of the Hsp70-Hsp90 multichaperone machine. *Cell*, *101*(2), 199-210. https://doi.org/10.1016/S0092-8674(00)80830-2

Sevigny, J., Chiao, P., Bussière, T., Weinreb, P. H., Williams, L., Maier, M., Dunstan, R., Salloway, S., Chen, T., Ling, Y., O'Gorman, J., Qian, F., Arastu, M., Li, M., Chollate, S., Brennan, M. S., Quintero-Monzon, O., Scannevin, R. H., Arnold, H. M., . . . Sandrock, A. (2016). The antibody aducanumab reduces Aβ plaques in Alzheimer's disease. *Nature*, *537*(7618), 50-56. https://doi.org/10.1038/nature19323

Shi, Y., Ghetti, B., Goedert, M., & Scheres, S. H. W. (2022). Cryo-EM structures of chronic traumatic encephalopathy tau filaments with PET ligand flortaucipir. 2022.2012.2015.520545. https://doi.org/10.1101/2022.12.15.520545

Shi, Y., Murzin, A. G., Falcon, B., Epstein, A., Machin, J., Tempest, P., Newell, K. L., Vidal, R., Garringer, H. J., Sahara, N., Higuchi, M., Ghetti, B., Jang, M. K., Scheres, S. H. W., & Goedert, M. (2021). Cryo-EM structures of tau filaments from Alzheimer's disease with PET ligand APN-1607. *Acta Neuropathologica*, *141*(5), 697-708. https://doi.org/10.1007/s00401-021-02294-3

Shi, Y., Zhang, W., Yang, Y., Murzin, A. G., Falcon, B., Kotecha, A., van Beers, M., Tarutani, A., Kametani, F., Garringer, H. J., Vidal, R., Hallinan, G. I., Lashley, T., Saito, Y., Murayama, S., Yoshida, M., Tanaka, H., Kakita, A., Ikeuchi, T., . . . Scheres, S. H. W. (2021). Structure-based classification of tauopathies. *Nature*, *598*(7880), 359-363. https://doi.org/10.1038/s41586-021-03911-7

Spillantini, M. G., & Goedert, M. (2013). Tau pathology and neurodegeneration. *The Lancet.Neurology*, *12*(6), 609-622. https://doi.org/10.1016/S1474-4422(13)70090-5

Stelzl, L. S., Pietrek, L. M., Holla, A., Oroz, J., Sikora, M., Köfinger, J., Schuler, B., Zweckstetter, M., & Hummer, G. (2022). Global Structure of the Intrinsically Disordered Protein Tau Emerges from Its Local Structure. *JACS Au*, *2*(3), 673-686. https://doi.org/10.1021/jacsau.1c00536

Sunde, M., & Blake, C. (1997). The structure of amyloid fibrils by electron microscopy and X-ray diffraction. *Advances in Protein Chemistry*, *50*, 123-159. https://doi.org/10.1016/s0065-3233(08)60320-4

Teunissen, C. E., Verberk, I. M. W., Thijssen, E. H., Vermunt, L., Hansson, O., Zetterberg, H., Van Der Flier, W. M., Mielke, M. M., & Del Campo, M. (2022). Blood-based biomarkers for Alzheimer's disease: towards clinical implementation. *The Lancet Neurology*, *21*(1), 66-77. https://doi.org/10.1016/s1474-4422(21)00361-6

Thal, D. R., von Arnim, C., Griffin, W. S., Yamaguchi, H., Mrak, R. E., Attems, J., & Upadhaya, A. R. (2013). Pathology of clinical and preclinical Alzheimer's disease. *European archives of psychiatry and clinical neuroscience*, *263 Suppl 2*, 137. https://doi.org/10.1007/s00406-013-0449-5

Van Dyck, C. H., Swanson, C. J., Aisen, P., Bateman, R. J., Chen, C., Gee, M., Kanekiyo, M., Li, D., Reyderman, L., Cohen, S., Froelich, L., Katayama, S., Sabbagh, M., Vellas, B., Watson, D., Dhadda, S., Irizarry, M., Kramer, L. D., & Iwatsubo, T. (2023). Lecanemab in Early Alzheimer's Disease. *New England Journal of Medicine*, *388*(1), 9-21. https://doi.org/10.1056/nejmoa2212948

Vassar, P. S., & Culling, C. F. (1959). Fluorescent stains, with special reference to amyloid and connective tissues. *Archives of Pathology*, *68*, 487-498.

Xia, C. F., Arteaga, J., Chen, G., Gangadharmath, U., Gomez, L. F., Kasi, D., Lam, C., Liang, Q., Liu, C., Mocharla, V. P., Mu, F., Sinha, A., Su, H., Szardenings, A. K., Walsh, J. C., Wang, E., Yu, C., Zhang, W., Zhao, T., & Kolb, H. C. (2013). [¹⁸ F]T807, a novel tau positron emission tomography imaging agent for Alzheimer's disease. *Alzheimer's & Dementia*, *9*(6), 666-676. https://doi.org/10.1016/j.jalz.2012.11.008

Yoshizaki, T., & Yamakawa, H. (1980). Dynamics of spheroid-cylindrical molecules in dilute solution. *Journal of Chemical Physics*, *72*, 57-69.

Zhang, W., Falcon, B., Murzin, A. G., Fan, J., Crowther, R. A., Goedert, M., & Scheres, S. H. (2019). Heparin-induced tau filaments are polymorphic and differ from those in Alzheimer's and Pick's diseases. *eLife*, *8*, 10.7554/eLife.43584. https://doi.org/10.7554/eLife.43584

Zhang, W., Tarutani, A., Newell, K. L., Murzin, A. G., Matsubara, T., Falcon, B., Vidal, R., Garringer, H. J., Shi, Y., Ikeuchi, T., Murayama, S., Ghetti, B., Hasegawa, M., Goedert, M., & Scheres, S. H. W. (2020). Novel tau filament fold in corticobasal degeneration. *Nature*, *580*(7802), 283-287. https://doi.org/10.1038/s41586-020-2043-0

Zheng, N., & Shabek, N. (2017). Ubiquitin Ligases: Structure, Function, and Regulation. *Annual Review of Biochemistry*, *86*, 129-157. https://doi.org/10.1146/annurev-biochem-060815-014922

Supplementary figures

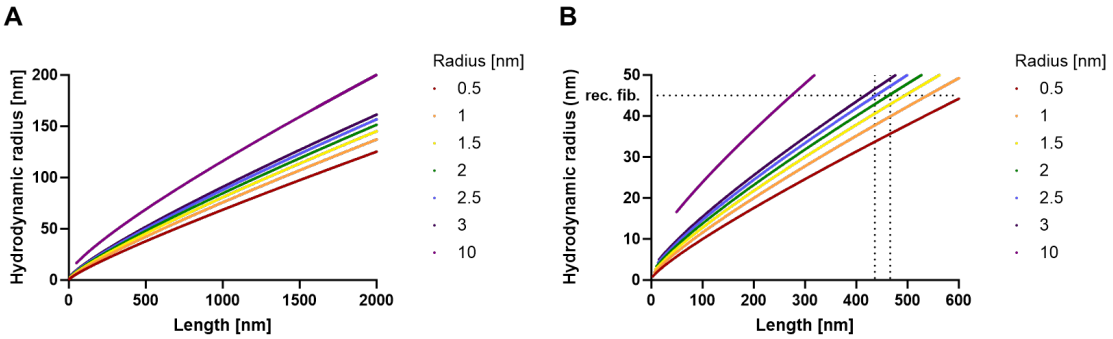

Supplementary Figure 1 **Correlation between Hydrodynamic Radius (R_h) and Fibril Length.** A) Model where the HR is plotted as a function of fibril length. Important is the effect of the radius of the monomer. B) An example of the HR found for recombinant Tau fibrils (Fig 5A), estimated to have a radius of 2-2.5 nm, corresponding to a fibril length of 436-466 nm.

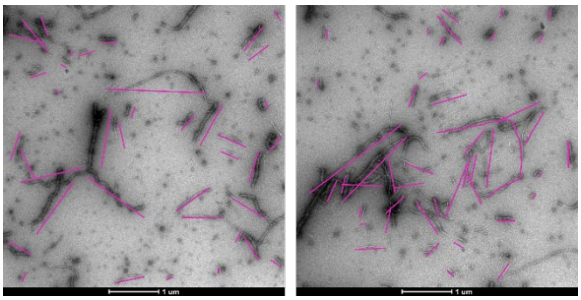

Supplementary Figure 2 **Fibrils counted to estimate the size of TauRD fibrils.** Two squares were assessed for the average fibril length of recombinant TauRD fibrils. All fibrils used for the assessment highlighted in purple. Fibrils not completely in square were excluded. For measurement, the scale of the detection technique was used. 89 fibrils were counted with an average length of 0.5 – 0.6 µM.

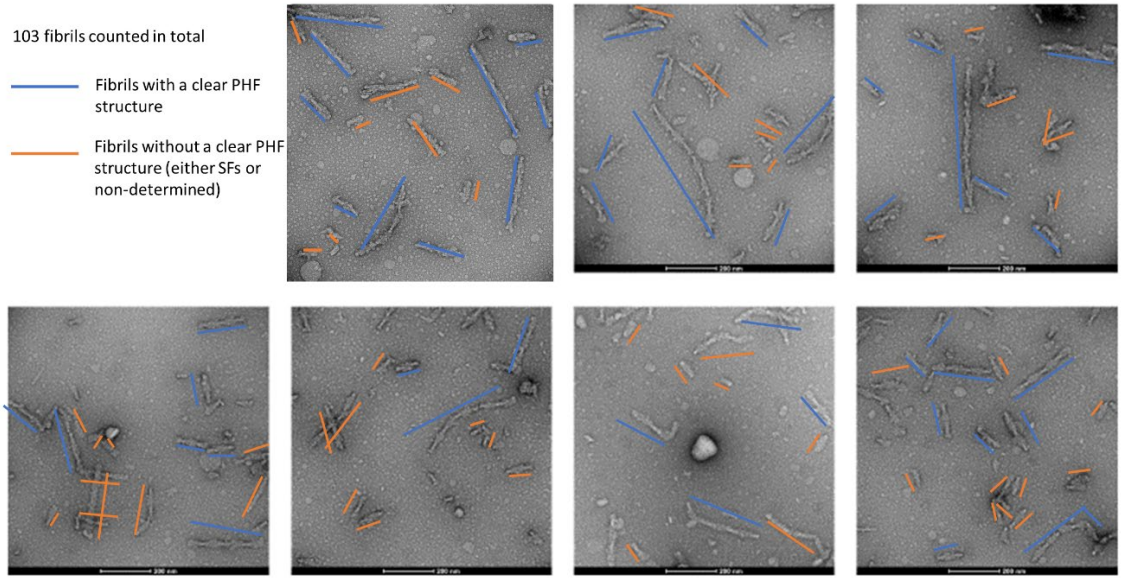

Supplementary Figure 3 **Fibrils counted to assess fibril length of Paired Helical Filaments (PHFs).** Seven different squares were used to count the presence of PHFs (blue) or Straight Filaments (SFs, orange) or structures with undefined structure (orange). PHFs were used as a tool to asses fibril length, as the turning element has a set length (340 layers needed with distance 0.47 nm between each layer). The average length of the PHFs had 2.7 twists, resembling a length around 450 nm.